




# HST STIS UV Spectroscopic Observations of the Protoplanetary Nebula Hen3-1475<sup>\*†</sup>

Xuan Fang<sup>1,2,6</sup> , Ana I. Gómez de Castro<sup>3</sup> , Jesús A. Toalá<sup>4</sup> , and Angels Riera<sup>5,7</sup> <sup>1</sup>Laboratory for Space Research, Faculty of Science, The University of Hong Kong, Pokfulam Road, Hong Kong, People's Republic of China; [fangx@hku.hk](mailto:fangx@hku.hk)<sup>2</sup>Department of Physics, Faculty of Science, The University of Hong Kong, Pokfulam Road, Hong Kong, People's Republic of China<sup>3</sup>AEGORA Research Group, Facultad de Ciencias, Universidad Complutense, E-28040, Madrid, Spain<sup>4</sup>Instituto de Radioastronomía y Astrofísica, UNAM Campus Morelia, Apartado postal 3-72, Morelia 58090, Michoacán, Mexico<sup>5</sup>Departament de Física i Enginyeria Nuclear, EUETIB, Universitat Politècnica de Catalunya, E-08036 Barcelona, Spain

Received 2018 July 21; revised 2018 September 15; accepted 2018 September 17; published 2018 October 1

## Abstract

We present UV spectra of the protoplanetary nebula (pPN) Hen 3-1475 obtained with the Space Telescope Imaging Spectrograph (STIS) on board the *Hubble Space Telescope* (HST). Our deep, low-dispersion spectroscopy enables monochromatic imaging of Hen 3-1475 in ultraviolet (UV) nebular emission lines, the first of such attempt ever made for a pPN. The high spatial resolution of STIS imaging allows an unprecedentedly sharp view of the S-shaped jet, especially the inner NW1 knot, which is resolved into four components in Mg II  $\lambda$ 2800. Through critical comparison with HST optical narrowband images, we found a negative radial velocity gradient in NW1, from  $-1550 \text{ km s}^{-1}$  on its innermost component to  $\sim -300 \text{ km s}^{-1}$  on the outermost. Despite their high radial velocities, these components of NW1 mostly show no obvious (or very small) proper motions, indicating that they might be quasi-stationary shocks near the tip of the conical flow along the collimated jet of Hen 3-1475.

*Key words:* ISM: jets and outflows – planetary nebulae: individual (Hen3-1475) – stars: AGB and post-AGB

## 1. Introduction

Planetary nebulae (PNe) exhibit a great variety of morphologies. The low occurrence of spherical symmetry is perplexing because most asymptotic giant branch (AGB) envelopes are spherical (e.g., Neri et al. 1998; Mauron et al. 2013). The transformation from a spherical AGB envelope to an aspherical PN begins at the protoplanetary nebula (pPN) phase, when the stellar temperature is still too low to photoionize the nebula. Collimated outflows as fast as  $400 \text{ km s}^{-1}$  have been detected in pPNe (Bujarrabal et al. 2001), and play a major role in PN shaping (Sahai & Trauger 1998). An even faster jet ( $630 \text{ km s}^{-1}$ ) was found in the young PN MyCn 18 (Miszalski et al. 2018). Binarity is believed to be responsible for jet formation, as recently observed in the symbiotic star RAqr (Schmid et al. 2017) and the AGB star YGem (Sahai et al. 2018).

Hen 3-1475 (a.k.a. the “Garden Sprinkler Nebula”), was first recognized as a transition object in the post-AGB phase (Parthasarathy & Pottasch 1989) and later found to have fast bipolar outflows (Riera et al. 1995). Since its nature as a pPN was settled, Hen 3-1475 has been imaged on several occasions

(Bobrowsky et al. 1995; Borkowski et al. 1997; Ueta et al. 2000; Borkowski & Harrington 2001). It has a highly collimated bipolar structure with an S-shaped string of point-symmetric, [N II]-bright knots extending over  $\sim 17''$  along the main axis (Figure 1). High-dispersion spectroscopy revealed high-velocity jets ( $1200 \text{ km s}^{-1}$ , Borkowski & Harrington 2001) and ultra-fast (up to  $2300 \text{ km s}^{-1}$ ) winds very close to the central star (Sánchez Contreras & Sahai 2001). To date, Hen 3-1475 is the only pPN with detected diffuse X-ray emission, a signature of stellar winds interactions (Sahai et al. 2003); this X-ray emission comes mostly from its brightest NW1<sup>8</sup> knot, whose emission is shock excited (Borkowski & Harrington 2001; Riera et al. 2003, 2006). Its outflows are being collimated into jets far away from the central star (Borkowski et al. 1997), but the collimation mechanism is not well understood. A time-dependent ejection velocity model with a period of 1500 years was proposed to explain its morphology and kinematics (Velázquez et al. 2004).

*International Ultraviolet Explorer* (IUE) detection of ultraviolet (UV) emission lines in Hen 3-1475 was only marginal due to dust obscuration (Gaubá & Parthasarathy 2003); however, the effects of shocks can be studied in the UV. Here we report on UV spectroscopy of Hen 3-1475 obtained with the *Hubble Space Telescope* (HST). After briefly revisiting jet propagation in Section 2, we introduce our HST observations in Section 3. Data analysis and discussion are presented in Section 4, and the summary and future plan in Section 5.

## 2. Jet Propagation of Hen 3-1475

Jet propagation of Hen 3-1475 was studied by Borkowski & Harrington (2001) based on 1996/1999 observations. We now investigate it using the F658N images obtained on 1999 September 9 (WFPC2/PC; prop. 7285, PI: J. P. Harrington)

\* Based on observations made with the NASA/ESA *Hubble Space Telescope*, obtained at the Space Telescope Science Institute, which is operated by the Association of Universities for Research in Astronomy, Inc., under NASA contract NAS 5-26555. The UV observations are associated with the HST GO program #13838.

† Dedicated to Dr. Angels Riera, who passed away on 2017 September 27 in Barcelona, Spain. Dr. Riera was the first to recognize the peculiar nature of Hen 3-1475.

<sup>6</sup> Visiting Astronomer, Key Laboratory of Optical Astronomy, National Astronomical Observatories, Chinese Academy of Sciences (NAOC), 20A Datun Road, Chaoyang District, Beijing 100101, P. R. China.

<sup>7</sup> Deceased.

<sup>8</sup> Following Borkowski et al. (1997), we hereafter refer the inner, middle, and outer pairs of knots in Hen 3-1475 as NW1/SE1, NW2/SE2, and NW3/SE3, respectively. See also Figure 1.

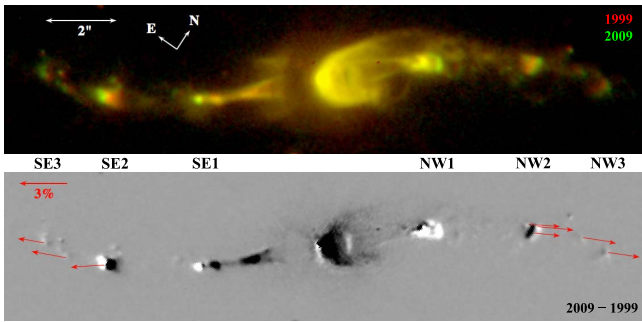


**Figure 1.** Top: *Hubble Space Telescope* (*HST*) F658N images of Hen 3-1475 obtained in 1999 (red) and 2009 (green). Bottom: residual F658N image (a 2009–1999 difference); red arrows overlaid show the expansion directions, with lengths proportional to fractional expansion (in percentage, as defined by Equation (2) in Fang et al. 2014).

and 2009 August 6 (WFC3; prop. 11580, PI: B. Balick). The WFPC2/PC ( $0''.050 \text{ pixel}^{-1}$ ) image was aligned, rebinned and scaled to WFC3 ( $0''.0396 \text{ pixel}^{-1}$ ) following the procedure described in Fang et al. (2014). The two images displayed together show obvious proper motion of the outer knots (NW2/SE2 and NW3/SE3), but it is *not obvious* in NW1/SE1 whose outer parts are much brighter in 2009 than in 1999 (Figure 1 top). This brightening may cause apparently large (but false) proper motion of NW1/SE1 (Figure 1, bottom). Proper motions of the outer knots are  $\sim 10\text{--}15 \text{ mas yr}^{-1}$ , corresponding to sky-projected velocities of  $230\text{--}360 \text{ km s}^{-1}$  (at a distance of 5 kpc, Riera et al. 1995; hereafter adopted); these are consistent with the measurements of Borkowski & Harrington (2001). The outer knots move almost *tangentially* along the S-shaped arms of Hen 3-1475 (Figure 1, bottom), unlike the purely radial (from the core) motions usually expected for the knots ejected from a precessing nozzle as proposed by Riera et al. (2003). The possible mechanism of such tangential motion is discussed in Section 4.2. Figure 1 also shows very small motion of the two inner cones (i.e., the limb-brightened edges of conical shocks; Borkowski et al. 1997) that originate from the central torus and “converge” at NW1/SE1.

### 3. STIS Observations

Long-slit UV spectra of Hen 3-1475 were obtained with the Space Telescope Imaging Spectrograph (STIS) on board the *HST* on 2015 June 11, under the GO program #13838 (PI: X. Fang, Cycle 22). First-order gratings G140L and G230L were used to obtain the far-UV (FUV) and near-UV (NUV) spectra, respectively. The STIS  $52'' \times 2''$  long slit was placed on the central core (R.A. =  $17^{\text{h}}45^{\text{m}}14^{\text{s}}.19$ , decl. =  $-17^{\circ}56'46''.9$ ) of Hen 3-1475 with a position angle (PA) of  $124^{\circ}.65$  along the nebular axis. All knots lie within the slit (Figure 2(a)). The observations were in the TIME-TAG mode, which allows us to scrutinize the data for periods of high airglow level. The instrument parameters and exposures are all summarized in Table 1, where we also present the actual angular resolutions (in arcsec) for the two grating modes as provided by the STIS Instrument Handbook.

The data were reduced and calibrated with the *HST* STIS pipeline. The long-slit low-dispersion spectroscopy enables *monochromatic imaging* of Hen 3-1475 on UV nebular emission lines (see the description in Section 4.1), while reducing the impact of the bright geocoronal  $\text{Ly}\alpha$  emission.

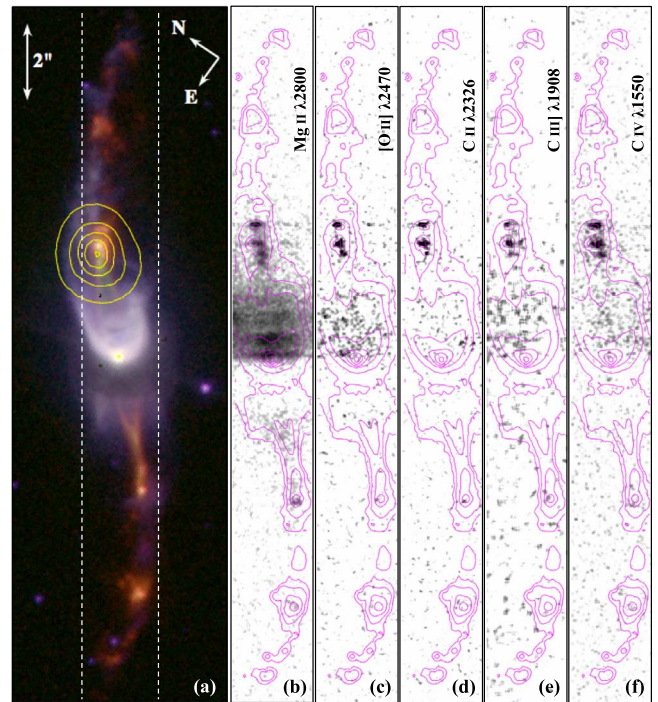


**Figure 2.** Panel (a): *HST* 2009 WFC3 color-composite image of Hen 3-1475 created with F658N (red), F656N (green), and F555W (blue) and overlaid with *Chandra* Advanced CCD Imaging Spectrometer (ACIS) X-ray emission contours (yellow; Obs. ID 2580; P.I.: R. Sahai). White dashed lines indicate the STIS  $52'' \times 2''$  long slit (PA =  $124^{\circ}.65$ ). Panels (b)–(f): STIS UV spectral-line images (see the legend by Fang et al. 2014) overlaid with WFC3 F658N emission contours (magenta); each panel is  $2'' \times 17''.2$  in size, displayed in negative grayscale and slightly smoothed to reduce noise.

Several emission lines of the fully calibrated spectra are demonstrated in Figure 2. The FUV spectrum includes N V  $\lambda\lambda 1239, 1242$  (all wavelengths in Å), C IV  $\lambda 1550$  (a blend of  $\lambda\lambda 1548, 1551$ ), He II  $\lambda 1640$ , and O III]  $\lambda\lambda 1661, 1666$ . In NUV we detected C III]  $\lambda 1908$ , C II  $\lambda 2326$ , [O II]  $\lambda 2470$  and Mg II  $\lambda 2800$  (a blend of  $\lambda\lambda 2795, 2803$ ). No fine-structure transition lines in any doublet detected in our low-dispersion spectra are spectroscopically resolved.

## 4. Results and Discussion

### 4.1. UV Morphology

The UV morphology of Hen 3-1475 is studied in conjunction with *HST* WFC3 images in the F656N and F658N filters that show the  $\text{H}\alpha$  and [N II]  $\lambda 6583$  emission, mostly from the jets and knots, which are presumably shock excited (Borkowski & Harrington 2001); the broadband images (e.g., F555W and F814W) show the continuum radiation, mostly scattered starlight. We created UV monochromatic images by first selecting in the STIS 2D spectrum regions centered on UV emission lines, and then carefully registered them with WFC3 images. The overall morphology of Hen 3-1475’s brightest regions (NW1/SE1 and the central reflection nebula), as outlined in optical emission, is visible in several UV lines (Figure 2). In the Mg II  $\lambda 2800$  spectral-line image, the NW1 knot is resolved into four components, hereafter named A, B, C, and D (from the inside out; Figures 3(a), (b)), with angular sizes of  $\sim 0''.12\text{--}0''.14$  along the jet axis; in the other UV lines, generally fainter than Mg II, only the three outer components, B, C, and D, are seen (Figures 2(b)–(f)). The SE1 knot seen in



**Table 1**  
HST STIS Observing Log

Detector	Grating	$\lambda_c$ (Å)	Spectral Range (Å)	Spectral Resolution (R)	Dispersion (Å pixel <sup>-1</sup> )	Spatial Scale (pixel <sup>-1</sup> )	Angular Resolution	$t_{\text{exp}}$ (s)
STIS/FUV-Multi-Anode Microchannel Array (MAMA)	G140L	1425	1150–1730	960–1440	0.58	0''0246	~0''07	2800
STIS/NUV-MAMA	G230L	2376	1570–3180	500–1010	1.55	0''0248	~0''06	2100

**Note.** Instrument parameters are adopted from <http://www.stsci.edu/hst/stis/design/gratings>.

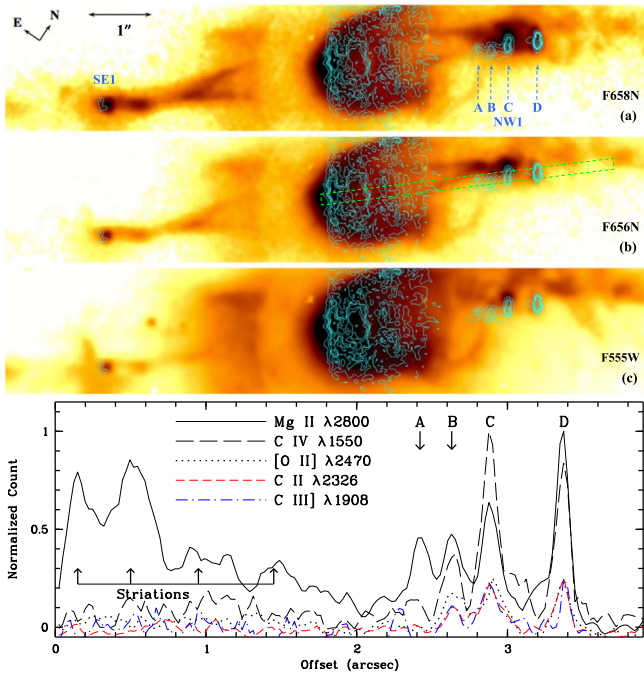


**Figure 3.** Top three panels: emission contours (cyan) of the STIS Mg II  $\lambda 2800$  line overlaid on the WFC3 F658N (a), F656N (b), and F555W (c) images showing the central  $2'' \times 10''$  region of Hen 3-1475. The NW1 knot is resolved into four components (A, B, C, and D, labeled in blue) in Mg II. The nebular core is saturated in all three filters to enhance lobe structures, including NW1/SE1 and the conical shocks. Bottom panel: emission profiles of different UV lines along a cut (green dashed rectangle in panel (b)) through the central star and the NW1 knot components, at PA =  $311^\circ$ ; positions of the four components of NW1 and the striations seen in Mg II emission (Figure 2(b)) are labeled. Emissions of [O II], C II and C III] are normalized and further scaled for easy comparison.

the UV could be the counterpart of the outermost D component.

The optical counterparts (in H $\alpha$ ) of the four UV components A, B, C, and D are located  $2''49$  ( $1''73$ -W,  $1''79$ -N),  $2''67$  ( $1''93$ -W,  $1''85$ -N),  $2''91$  ( $2''07$ -W,  $2''04$ -N), and  $3''30$  ( $2''47$ -W,  $2''19$ -N) from the central star, respectively. B, C, and D are elongated (in the dispersion direction) in Mg II; this elongation is obvious in B and C, which are compact in H $\alpha$ . D comprises two subcomponents in H $\alpha$  that are  $\sim 0''15$  apart and stretch by  $0''32$ , similar to the size in the UV. The NW conical shock “converges” on A (Figures 4(a), (b)), the most compact (radius  $\sim 0''06$ ) among the four UV components of NW1. Elongation of the NW1 components in the UV may be caused by large, internal negative radial velocity gradients (Borkowski & Harrington 2001).

Along the (spectral) dispersion direction, the four components of NW1 seem to be displaced with respect to their optical

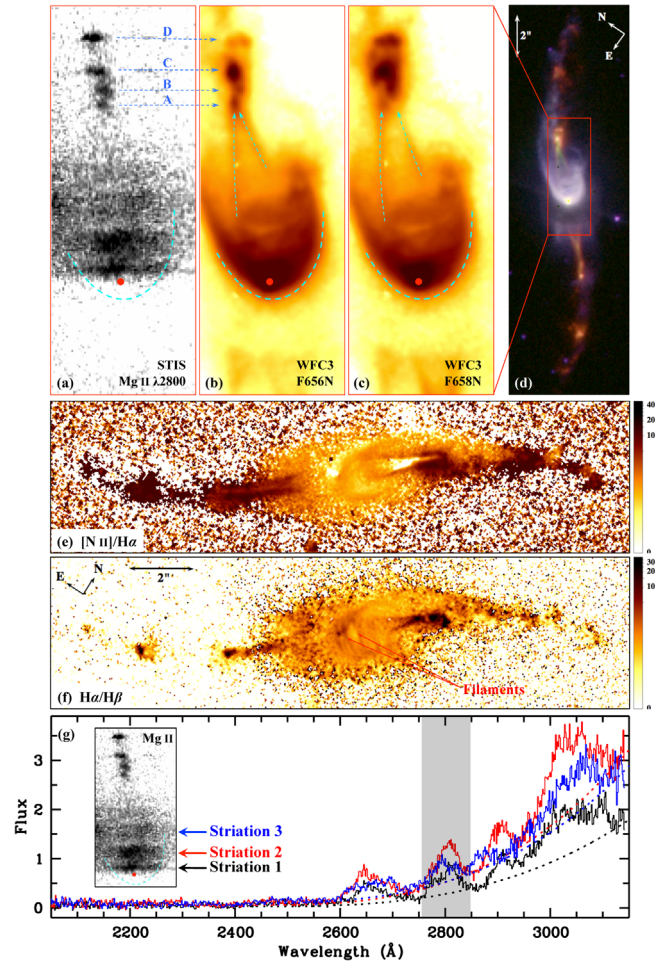


**Figure 4.** Close-up view of the central  $2'' \times 5''/4$  region of Hen 3-1475 in Mg II  $\lambda 2800$  (a), H $\alpha$  (b), and [N II] (c); the four components of the NW1 knot are labeled. The slightly curved conical converging shock and the outer boundary of NW lobe are delineated (b, c). Red dot marks the position of the central star. Panel (d) is the same as Figure 2(a). Panels (e) and (f) are [N II]/H $\alpha$  and H $\alpha$ /H $\beta$  ratio images, respectively, both displayed in inverted false color (i.e., dark regions in panel (e) have strong [N II] emission relative to H $\alpha$  and accompanied by color bars in logarithmic scale. Panel (g): Extracted 1D NUV spectra of the three inner striations as indicated by color-coded arrows on an inset of the Mg II  $\lambda 2800$  spectral-line image (same as panel (a)); the dotted curves are polynomial fits of the corresponding underlying continua; the Mg II emission feature is marked by the gray-shaded area. Flux is in units of  $10^{-14}$  erg cm<sup>-2</sup> s<sup>-1</sup> Å<sup>-1</sup>.

counterparts; we discuss this in Section 4.2. Along the slit direction, positions of A, B, and C in the UV are unchanged compared to their counterparts in H $\alpha$ , which is consistent with the very little expansion of NW1 that we found through comparison of the 1999/2009 F658N images (see Section 2). Component D and SE1 in the UV are slightly outside their H $\alpha$

counterparts (Figure 3(b)) due to jet expansion/propagation since 2009. The position of D in Mg II is shifted outward (i.e., toward NW) by  $0''.069$  from its position in H $\alpha$ , which corresponds to a proper motion of  $11.8 \text{ mas yr}^{-1}$ , or  $\sim 280 \text{ km s}^{-1}$ . Similarly, SE1 in Mg II is displaced from its position in H $\alpha$  by  $0''.091$ , corresponding to  $\sim 15.5 \text{ mas yr}^{-1}$ , or  $\sim 360 \text{ km s}^{-1}$ .

In the UV spectrum,  $<2''$  from the central star, there are four “stripes” (or striations) that are more prominent near the red end of the STIS NUV-MAMA spectrum (Figure 2(b)). These striations are only detected in the NW lobe, and seem to spatially align with the optical features at corresponding locations: the hollow U-shaped “bowls” near the nucleus of Hen 3-1475 also seem striated in the optical (Figures 4(b), (c)). The central region of Hen 3-1475 is dominated by the scattered stellar light as shown in the *HST* STIS G750M spectrum (Borkowski & Harrington 2001, Figure 2 therein). Along the jet axis, the four UV striations in the NW lobe are  $\sim 0''.13$ ,  $0''.5$ ,  $0''.95$  and  $1''.43$  from the central star (Figure 3, bottom).

#### 4.2. Jet Kinematics and Shocks

Whereas the positions of A, B, and C in the UV along the slit direction are consistent with those of their counterparts in H $\alpha$ , there is a noticeable shift along the dispersion direction of the UV spectrum (Figure 3(b)). Given that the NW jet of Hen 3-1475 has high approaching speeds (Borkowski & Harrington 2001; Riera et al. 2003), it is plausible to attribute these displacements to Doppler shift.<sup>9</sup> Indeed, A, B, and C are shifted blueward in the UV spectrum by 9.4, 7.2 and 6.7 pixels which, if entirely due to Doppler shift, correspond to radial velocities of  $-1550 \pm 160$ ,  $-1200 \pm 330$  and  $-1100 \pm 400 \text{ km s}^{-1}$ , respectively. The systemic radial velocity of Hen 3-1475 ( $+40 \text{ km s}^{-1}$ , Borkowski & Harrington 2001) is within the velocity errors. Although the outermost component D, as well as SE1 in the UV, seems to align with its optical counterpart along the spectral direction, we cannot rule out the possibility that D also has a high approaching speed, given its extension and the low spectral resolution of G230L. This sets an upper limit of  $\lesssim 310 \text{ km s}^{-1}$  for the approaching speed of D. Adopting this radial speed and the sky-projected velocity of D ( $\sim 280 \text{ km s}^{-1}$ , see Section 4.1), we deduce a jet inclination ( $i$ , with respect to the line of sight)  $\gtrsim 42^\circ$ , which is consistent with the estimate of (Borkowski & Harrington 2001,  $i = 40^\circ$ ). Adopting  $i = 40^\circ$ , we corrected the velocities of A, B, C, and D to be  $\sim 2000$ ,  $1600$ ,  $1400$ , and  $\lesssim 400 \text{ km s}^{-1}$ , respectively.

Both the [N II] and H $\alpha$  emission lines in the *HST* STIS G750M optical spectroscopy (in 1999; Borkowski & Harrington 2001) show an increase in radial velocity from the base region of the NW conical shock, reaching a maximum blueshift of  $-910 \text{ km s}^{-1}$  at the cone tip (i.e., component A), and followed by a small drop (by  $\sim 110 \text{ km s}^{-1}$ ) near the cone tip, and continuous decrease in velocity through C to D. This small drop in velocity near the cone tip is reflected by the velocity difference between A and B in the UV. Our radial velocities derived for the UV components of NW1, although higher than those found in the STIS G750M spectrum, generally follow the same trend

<sup>9</sup> In [N II] emission there are NW1 components that seem to spatially coincide better, along the SW edges, with the corresponding Mg II ones than H $\alpha$  does; this indicates that the offsets of these UV components with respect to H $\alpha$  might be, at least partially, due to Mg II emission arising from the [N II]-emitting gas toward the SW from the H $\alpha$  emission. An in-depth analysis of the UV+optical data is needed to confirm this.

(i.e., decreasing from the inside out), indicating a sequence of negative speed changes within NW1. The jet might have been accelerated since 1999 possibly because the central star has become hotter.

If the NW1 components are moving clumps along the jet, the sky-projected velocities of A, B, C, and D should be  $\sim 1300$ ,  $1000$ ,  $900$ , and  $\lesssim 260 \text{ km s}^{-1}$  (adopting the above radial velocities and  $i = 40^\circ$ ), corresponding to proper motions of  $\sim 55$ ,  $42$ ,  $38$  and  $\lesssim 12 \text{ mas yr}^{-1}$ , respectively. However, A, B, and C are actually unchanged in positions, whereas D and SE1 show small radial displacements from their positions in the 2009 H $\alpha$  image (Figure 3(b); see Section 4.1). Such a spatio-kinematic pattern of NW1 seems to resemble quasi-stationary shocks: A, B, C, and D may actually be shock interfaces where the outflowing gas moves through with high speeds, and have no (or very small) measurable proper motions; each of these clumpy shocks may brighten or fade in time owing to variations in density or speed of the gas flow. If A, B, C, and D are indeed the locations of shocks, the gas flow should be slowed down at each of these shocks as some kinetic energy is converted into heat that locally excites line emission (B. Balick 2018, private communication). The negative radial velocity gradient in NW1 may thus be explained as a series of speed losses of the (possibly unstable) flow as it propagates outward along the jet. This interpretation, although plausible, is still speculative and needs careful assessment with comprehensive hydrodynamic simulations.

The outer pair of knots (NW2/SE2 and NW3/SE3) in Hen 3-1475 was previously proposed to be fast-moving “bullets”; but their almost tangential motion along the S-shaped arms (Figure 1, bottom; see also Section 2) suggests that this is probably not the case. One sensible interpretation is that these outer knots are actually bright spots along the curved arms, which may be faint lobe walls projected on the sky; these bright spots are produced due to the Kelvin–Helmholtz instabilities as excited by the fast streamlines flowing over the surface of lobe walls.

We analyzed the archival *HST* STIS G750L spectrum and found that the optical line ratios (e.g., [O II]/H $\beta$ , [O III]/H $\beta$ , [S II]/H $\alpha$ ) from the NW1 knot are roughly consistent with the predicted values of a bow-shock model at  $200 \text{ km s}^{-1}$  (Hartigan et al. 1987); this analysis will be presented separately (X. Fang et al. 2018, in preparation). The high-velocity jet impinges on the slower AGB wind, creating shocks as delineated by the [N II]/H $\alpha$  ratio (Figure 4(e)): the three pairs of knots, as well as the two limb-brightened inner cones, are enhanced in [N II] emission (although we are aware that at least for SE1, the F658N filter may be contaminated by redshifted H $\alpha$ ). Within the NW lobe, there are filaments enhanced in the H $\alpha$ /H $\beta$  ratio (Figure 4(f)); they may not be due to higher local extinction but actually related to variation in shock speed that causes locally enhanced temperature and/or density, which results in departure from the Case B recombination of hydrogen. The NW conical shock is slightly curved before it converges (Figures 4(b), (c)), an effect possibly due to interaction with the lobe walls, which are bright in scattered lights as seen in F555W (Figure 4(d)). The SE conical shock is also curved in optical line emission.

For each of the four striations within the NW lobe, its 1D NUV spectrum is composed of a smooth continuum overlaid by several emission features, one of them being Mg II  $\lambda 2800$  (see Figure 4(g) for 1D spectra of the inner three, namely



Striations 1, 2, and 3). The smooth continuum could be the scattered starlight, while the broad UV emission features may come from fast stellar outflows. The innermost UV striation is not located exactly on the central star, but offset by  $0''.13$  (probably due to obscuration by the central dusty torus), corresponding to  $\sim 9.7 \times 10^{15}$  cm; the half-width (FWHM/2) of Mg II emission is  $\sim 22 \text{ \AA}$ , corresponding to a radial velocity gradient up to  $2360 \text{ km s}^{-1}$ . These two quantities are consistent with both location ( $\sim 10^{16}$  cm) and velocity ( $\sim 2300 \text{ km s}^{-1}$ ) of the ultra-fast “pristine” post-AGB outflow found by Sánchez Contreras & Sahai (2001). We cannot rule out the possibility that such UV spread/broadening might also be (at least partially) due to spatial extent; but the broadening of emission features on the innermost layer (Striation 1) can be due to kinematics because its Mg II emission seems to extend beyond the U-shaped boundary of the NW lobe (Figure 4(a)).

#### 4.3. Physical Conditions within the NW1 Knots

The exact location of X-ray emission in NW1 is still unclear; although it seems to peak around the cone tip (Figure 2(a)), this might be an effect of heavy smoothing of the low-photon counting *Chandra* data. If X-ray emission comes from the component A, the simultaneous presence of X-ray, UV, and optical emission suggests that A is a cooling region of shocked gas with very strong temperature gradients. However, A is spatially unresolved in our UV monochromatic imaging, given that its angular size is comparable to the angular resolution of the STIS/NUV-MAMA detector ( $\sim 0''.06$ ; Table 1). The physical conditions within the NW1 knots will be assessed by a re-analysis of the X-ray data and substantiated with the UV and optical emission line ratios to derive shock properties (J. A. Toalá et al. 2018, in preparation).

Using Equation (1) of Gruendl et al. (2004) and the observed Mg II  $\lambda 2800$  line flux ( $5.2 \times 10^{-14} \text{ erg cm}^{-2} \text{ s}^{-1}$ ), we estimate a density of  $\sim 10^5 \text{ cm}^{-3}$  for component A. Here an extinction of  $A_V \sim 3.7$  magnitude (Riera et al. 1995) and the solar abundance (Mg/H =  $3.98 \times 10^{-5}$ , Asplund et al. 2009) were adopted; we also assume a maximum ionization fraction  $\text{Mg}^+/\text{Mg} = 0.69$  at  $T_e \approx 15,800 \text{ K}$  in ionization equilibrium (Shull & Van Steenberg 1982), and a filling factor of 1. Using the same assumptions above, we estimate densities of  $\sim 50,000\text{--}60,000 \text{ cm}^{-3}$  in B, C, and D. These estimates of the density from the UV-emitting region in NW1 are much higher than the electron density derived from the [S II]  $\lambda 6716/\lambda 6731$  ratio ( $\sim 3000 \text{ cm}^{-3}$ , Riera et al. 2006), suggesting different physical conditions in the UV, optical, and X-ray emission regions (especially in component A).

### 5. Summary and Future Work

We report on monochromatic imaging of Hen 3-1475 in UV nebular emission lines obtained through the *HST* STIS UV long-slit spectroscopy; this is the first of such attempt ever made for a PPN. We have analyzed the UV morphology of Hen 3-1475, in conjunction with archival *HST* optical data. The high spatial resolution of STIS UV imaging resolves the NW1 knot near the tip of the inner conical shock in Hen 3-1475 into four components in the Mg II  $\lambda 2800$  spectral-line image. These four UV components are distributed roughly along the jet axis with slight curvature; similar configuration also seems to exist near the SE cone. Compared to their optical counterparts, the four





components of the NW1 knot are mostly blueshifted due to their high (approaching) radial velocities, from  $-1550 \text{ km s}^{-1}$  on the innermost component to  $\sim -300 \text{ km s}^{-1}$  on the outermost one. Despite their high radial velocities, the four components of NW1 show no obvious proper motions through the period of two-decade *HST* observations, indicating that they might be quasi-stationary shocks where fast gas flows through. Given this interpretation, the negative radial velocity gradient found in NW1 might be explained as successive speed losses of the fast jet as it propagates outward, losing kinetic energy at the shock sites that are now identified as the four UV components of NW1. Moreover, through proper motion studies we found that the outer pairs of knots (NW2/SE2 and NW3/SE3) of Hen 3-1475 are moving almost tangentially along the S-shaped arms, which indicates that they may not be fast-moving “bullets” as previously suggested, but bright spots induced by Kelvin–Helmholtz instabilities.

The extremely fast conical outflow with the knotty structure near its vortex makes Hen 3-1475 unique from all other pPNe and young PNe so far observed. This Letter is mostly descriptive. Follow-up studies of this object, in particular jet collimation and interaction with the ambient outflowing AGB gas, based on multi-wavelength (X-ray, UV, optical, infrared) observations and utilizing state-of-the-art (magneto)hydrodynamic simulations, will be carried out (X. Fang et al. 2018, in preparation). Given that Hen 3-1475 is in rapid evolution, which causes drastic change in morphology and physical conditions, close monitoring of this PPN with high spatial resolution is essential in order to better understand its jet formation/collimation and more interestingly, nature of the central star (possibly a binary) and the circumstellar/circumbinary environment, such as dust, the disk, and the magnetic field.

We thank the referee, Jacco van Loon, for very constructive suggestions that greatly improved this article. We thank Martín A. Guerrero and Bruce Balick for in-depth discussion and valuable suggestions during paper drafting and revision. We also thank Albert A. Zijlstra and Vincent Icke for comments and suggestions. J.A.T. is funded by UNAM DGAPA PAPIIT project IA100318. A.I.G.d.C. acknowledges support from the Spanish Ministry of Economy and Competitiveness through grants ESP2014-54243-R and ESP2015-68908-R. X.F. acknowledges the support and hospitality of the IAA-CSIC for an academic visit in 2017 September, during which this article was discussed and drafted.

Facility: *HST* (STIS).

#### ORCID iDs

Xuan Fang  <https://orcid.org/0000-0002-3981-7355>  
 Ana I. Gómez de Castro  <https://orcid.org/0000-0002-3598-9643>  
 Jesús A. Toalá  <https://orcid.org/0000-0002-5406-0813>  
 Angels Riera  <https://orcid.org/0000-0002-0149-3690>

#### References

- Asplund, M., Grevesse, N., Sauval, A.-J., & Scott, P. 2009, *ARA&A*, 47, 481  
 Bobrowsky, M., Zijlstra, A. A., Grebel, E. K., et al. 1995, *ApJL*, 446, L89  
 Borkowski, K. J., Blondin, J. M., & Harrington, J. P. 1997, *ApJL*, 482, L97  
 Borkowski, K. J., & Harrington, J. P. 2001, *ApJ*, 550, 778  
 Bujarrabal, V., Castro-Carrizo, A., Alcolea, J., & Sánchez Contreras, C. 2001, *A&A*, 377, 868  
 Fang, X., Guerrero, M. A., Marquez-Lugo, R. A., et al. 2014, *ApJ*, 797, 100  
 Gauba, G., & Parthasarathy, M. 2003, *A&A*, 407, 1007  
 Gruendl, R. A., Chu, Y.-H., & Guerrero, M. A. 2004, *ApJL*, 617, L127

- Hartigan, P., Raymond, J., & Hartmann, L. 1987, [ApJ](#), **316**, 323
- Mauron, N., Huggins, P. J., & Cheung, C.-L. 2013, [A&A](#), **551**, A110
- Miszalski, B., Manick, R., Mikołajewska, J., et al. 2018, [PASA](#), **35**, 27
- Neri, R., Kahane, C., Lucas, R., et al. 1998, [A&AS](#), **130**, 1
- Parthasarathy, M., & Pottasch, S. R. 1989, [A&A](#), **225**, 521
- Riera, A., Binette, L., & Raga, A. C. 2006, [A&A](#), **455**, 203
- Riera, A., García-Lario, P., Manchado, A., Bobrowsky, M., & Estalella, R. 2003, [A&A](#), **401**, 1039
- Riera, A., García-Lario, P., Manchado, A., Pottasch, S. R., & Raga, A. C. 1995, [A&A](#), **302**, 137
- Sahai, R., Kastner, J. H., Frank, A., Morris, M., & Blackman, E. G. 2003, [ApJL](#), **599**, L87
- Sahai, R., Sánchez Contreras, C., Mangan, A. S., et al. 2018, [ApJ](#), **860**, 105
- Sahai, R., & Trauger, J. T. 1998, [AJ](#), **116**, 1357
- Sánchez Contreras, C., & Sahai, R. 2001, [ApJL](#), **553**, L173
- Schmid, H. M., Bazzon, A., Milli, J., et al. 2017, [A&A](#), **602**, A53
- Shull, J. M., & Van Steenberg, M. 1982, [ApJS](#), **48**, 95
- Ueta, T., Meixner, M., & Bobrowsky, M. 2000, [ApJ](#), **528**, 861
- Velázquez, P. F., Riera, A., & Raga, C. 2004, [A&A](#), **419**, 991